AIAA JOURNAL
Vol. 45, No. 7, July 2007

Optimum Shape Design for Unsteady Flows with Time-Accurate Continuous and Discrete Adjoint Methods

Siva K. Nadarajah*
McGill University, Montreal, Quebec H3A 2S6, Canada
and
Antony Jameson†
Stanford University, Stanford, California 94305

DOI: 10.2514/1.24332

This paper presents an adjoint method for the optimal control of unsteady flows. The goal is to develop the continuous and discrete unsteady adjoint equations and their corresponding boundary conditions for the time-accurate method. First, this paper presents the complete formulation of the time-dependent optimal design problem. Second, we present the time-accurate unsteady continuous and discrete adjoint equations. Third, we present results that demonstrate the application of the theory to a two-dimensional oscillating airfoil. The results are compared with a multipoint approach to illustrate the added benefit of performing full unsteady optimization.

Nomenclature

A = flux Jacobian matrix
$\mathcal{B}$ = boundary
b = boundary velocity component
$\bar{c}$ = chord length
D = artificial dissipation flux
E = internal energy
F = Euler numerical flux vector
f = Euler flux vector
$\mathcal{G}$ = gradient
I = cost function
i, j = cell indices
M = Mach number
N = outward-facing normal
p = pressure
R = residual
$\mathcal{S}$ = shape function
S = face areas of the computational cell
s = arc length
T = time period
t = time
t_f = final time
u = velocity (physical domain)
V = cell volume
w = state vector
x = coordinates (physical domain)
α = angle of attack
ϵ = adjustable constant for artificial dissipation scheme
λ = step size
ξ = coordinates (computational domain)
ρ = density
ψ = Lagrange multiplier
ω_r = reduced frequency

Presented as Paper 5436 at the 9th AIAA/ISSMO Symposium on Multidisciplinary Analysis and Optimization Conference, Atlanta, GA, 4–6 September 2002; received 29 March 2006; revision received 29 November 2006; accepted for publication 18 January 2007.

*Assistant Professor, Computational Fluid Dynamics Lab, Department of Mechanical Engineering, 688 Sherbrooke Street West, Room 711; siva.nadarajah@mcgill.ca.

†Thomas V. Jones Professor of Engineering, Department of Aeronautics Astronautics, Durand Building, 496 Lomita Mall. Fellow AIAA.

I. Introduction

In THE past decade, aerodynamic shape optimization has been the focus of attention due largely to advanced algorithms that have allowed researchers to calculate gradients cheaply and efficiently. The majority of work in aerodynamic shape optimization has been focused on the design of aerospace vehicles in a steady flow environment. Investigators have applied these advanced design algorithms, particularly the adjoint method, to numerous problems, ranging from the design of two-dimensional airfoils to full aircraft configurations to decrease drag, increase range, and reduce sonic boom [1–11]. These problems were tackled using many different numerical schemes on both structured and unstructured grids [12–15].

Unlike fixed-wing aircraft, helicopter rotors and turbomachinery blades operate in unsteady flows and are constantly subjected to unsteady loads. Therefore, optimal control techniques for unsteady flows are needed to improve the performance of helicopter rotors and turbomachinery and to alleviate the unsteady effects that contribute to flutter, buffeting, poor gust and acoustic response, and dynamic stall.

Recently, the design of blade profiles using unsteady techniques was attempted. Diverse methods were employed in the design of rotorcraft and turbomachinery blades. The following are a selected number of papers on this topic. Ghayour and Baysal [16] solved the unsteady transonic small-disturbance equation and its continuous adjoint equation to perform an inverse design at Mach 0.6. Aerodynamic shape optimization of rotor airfoils in an unsteady viscous flow was attempted by Yee et al. [17] using a response-surface methodology. Here the authors used an upwind-biased-factorized implicit numerical scheme to solve the Reynolds-averaged Navier–Stokes equations with a Baldwin–Lomax turbulence model. A response-surface methodology was then employed to optimize the rotor blade. The objective function was a sum of the L/D at three different azimuth angles and was later redefined to include unsteady aerodynamic effects. Florea and Hall [18] modeled a cascade of turbomachinery blades using the steady and time-linearized Euler equations. Gradients for aeroelastic and aeroacoustic objective functions were then computed using the discrete adjoint approach. Both the flow and adjoint equations were solved using a finite volume Lax–Wendroff scheme. The gradients were then used to improve the aeroelastic stability and acoustic response of the airfoil.

Traditionally, a multipoint design approach is one possible technique for the optimization of blade profiles in an unsteady flow environment. This approach only requires a small extension of a steady flow design code to redesign a blade or airfoil profile for multiple flow conditions. Because the steady flow equations are used to design the blades, uncertainties still prevail surrounding the performance of these blades in an unsteady flow environment.

In this paper, we develop a framework in which to perform two major tasks: first, to perform sensitivity analysis in a nonlinear unsteady flow environment; second, to further modify the shape of the object to achieve the objective of the design using a full unsteady optimization method based on control theory. Optimal control of time-dependent trajectories is generally complicated by the need to solve the adjoint equation in reverse time from a final boundary condition using information from the trajectory solution, which in turn depends on the control derived from the adjoint solution. In this work, we extend the adjoint method to unsteady periodic flows using a time-accurate approach. The time-accurate unsteady adjoint equations are based on Jameson's [19] cell-centered multigrid-driven fully implicit scheme with upwind-biased, blended, first- and third-order artificial-dissipation fluxes.

The goal of this research is to develop both the time-accurate continuous and discrete adjoint equations and use them in the redesign of the RAE 2822 airfoil undergoing a pitching oscillation to achieve lower time-averaged drag while keeping the time-averaged lift constant. This technique is compared with the multipoint and steady adjoint approaches to gauge the effectiveness of the method.

II. Governing Equations

The Euler equations for a rigidly translating control volume Ω, defined by boundary $\partial\Omega$ with an outward-facing normal N, can be written in integral form as

$$\frac{d}{dt}\iint_{\Omega} w\,dx_1\,dx_2 + \oint_{\partial\Omega} f_i N_i\,ds = 0 \tag{1}$$

The state vector w and a component of the inviscid flux vector, f_i, can be written as

$$w = \begin{Bmatrix} \rho \\ \rho u_1 \\ \rho u_2 \\ \rho E \end{Bmatrix}, \qquad f_i = \begin{Bmatrix} \rho(u_i - b_i) \\ \rho u_1(u_i - b_i) + \delta_{1i}p \\ \rho u_2(u_i - b_i) + \delta_{2i}p \\ \rho E(u_i - b_i) + pu_i \end{Bmatrix}$$

In these equations, x_1 and x_2 are the Cartesian coordinates; u_i and b_i are the Cartesian velocity components of the fluid and boundary, respectively; and E is the total energy. The results presented in this paper are based on transonic flow calculations in which the ideal gas equation is applicable. Consequently, the pressure can be expressed as

$$p = (\gamma - 1)\rho\left\{E - \tfrac{1}{2}(u_i u_i)\right\}$$

A. Numerical Discretization of Governing Equations

A finite-volume methodology is used to discretize the integral form of the conservation laws. When using a discretization on a body-conforming structured mesh, it is useful to consider a transformation to the computational coordinates ξ_1 and ξ_2, defined by the metrics

$$K_{ij} = \left[\frac{\partial x_i}{\partial \xi_j}\right], \qquad J = \det(K), \qquad K_{ij}^{-1} = \left[\frac{\partial \xi_i}{\partial x_j}\right]$$

The simulations contained in this research are restricted to rigid mesh translation. Consequently, the volumetric integral from Eq. (1) can be approximated as the product of the cell volume and the temporal derivative of the solution at the cell center. The Euler equations can then be written in computational space as

$$V\frac{\partial w}{\partial t} + \frac{\partial F_i}{\partial \xi_i} = 0 \tag{2}$$

where the convective flux is now defined with respect to the computational cell faces by $F_i = S_{ij}f_j$, and the quantity $S_{ij} = JK_{ij}^{-1}$ represents the projection of the ξ_i cell face along the x_j axis. When Eq. (2) is formulated for each computational cell, a system of first-order ordinary differential equations is obtained. Equation (2) can then be written for each computational cell in semidiscrete form as

$$V\frac{\partial w}{\partial t} + R(w)_{i,j} = 0 \tag{3}$$

where

$$R(w)_{ij} = \frac{\partial F_1}{\partial \xi_1} + \frac{\partial F_2}{\partial \xi_2} = f_{i+\frac{1}{2},j} - f_{i-\frac{1}{2},j} + f_{i,j+\frac{1}{2}} - f_{i,j-\frac{1}{2}} \tag{4}$$

The $\pm\frac{1}{2}$ notation indicates that the quantity is calculated at the flux faces. To stabilize the scheme, a blended mix of first- and third-order fluxes first introduced by Jameson et al. [20] is added to the convective flux at each cell face and can be defined as

$$\begin{aligned} d_{i+\frac{1}{2},j} &= \epsilon^2_{i+\frac{1}{2},j}(w_{i+1,j} - w_{i,j}) \\ &\quad - \epsilon^4_{i+\frac{1}{2},j}(w_{i+2,j} - 3w_{i+1,j} + 3w_{i,j} - w_{i-1,j}) \end{aligned} \tag{5}$$

The first term in Eq. (5) is the first-order diffusion term, where $\epsilon^2_{i+\frac{1}{2},j}$ is proportional to the normalized second derivative of pressure. This term is dominant in the vicinity of shocks and serves to damp oscillations and overshoots associated with this discontinuity in the solution field. The $\epsilon^4_{i+\frac{1}{2},j}$ coefficient scales the magnitude of the third-order dissipative flux. The coefficient is scaled so that it becomes the dominant term away from the shock, eliminating the odd–even decoupling associated with central-difference schemes.

The time-derivative term can be approximated by a kth-order implicit backward-difference formula (BDF) such as

$$\frac{d}{dt} = \frac{1}{\Delta t}\sum_{q=1}^{k}\frac{1}{q}[\Delta^-]^q \tag{6}$$

where $\Delta^- = w^{n+1}_{i,j} - w^n_{i,j}$. A second-order expansion of Eq. (6) will result in the following equation for the semidiscrete form (3) of the governing equations:

$$V_{i,j}\left[\frac{3}{2\Delta t}w^{n+1}_{i,j} - \frac{2}{\Delta t}w^n_{i,j} + \frac{1}{2\Delta t}w^{n-1}_{i,j}\right] + R\left(w^{n+1}_{i,j}\right) = 0 \tag{7}$$

Equation (7) represents a set of highly nonlinear, coupled, ordinary differential equations and can be solved at each time step using the explicit multistage modified Runge–Kutta scheme. We define a new modified residual $R^*(w_{i,j})$ as

$$R^*(w_{i,j}) = V_{i,j}\left[\frac{3}{2\Delta t}w^{n+1}_{i,j} - \frac{2}{\Delta t}w^n_{i,j} + \frac{1}{2\Delta t}w^{n-1}_{i,j}\right] + R\left(w^{n+1}_{i,j}\right) \tag{8}$$

where the modified residual $R^*(w_{i,j})$ is the sum of the steady-state residual and a source term that originates from the second-order discretization of the time derivative. The modified residual is then marched to pseudosteady state in a fictitious time t^*, as follows:

$$\frac{dw_{i,j}}{dt^*} + R^*(w_{i,j}) = 0$$

The procedure advances the solution forward in time from the $t = n\Delta t$ to $t = (n+1)\Delta t$. The final time-accurate solution will be composed of a sequence of pseudotime steady-state solutions.

III. General Formulation of the Time-Dependent Optimal Design Problem

The aerodynamic properties that define the cost function are functions of the flowfield variables, w, and the physical location of the boundary, which may be represented by the function $\mathcal{S}$. We then introduce the cost function:

$$I = \frac{1}{T}\int_0^{t_f} \mathcal{L}(w, \mathcal{S})\,\mathrm{d}t + \mathcal{M}[w(t_f)] \tag{9}$$

The cost function is a sum of a time-averaged function $\mathcal{L}(w, \mathcal{S})$ and a function $\mathcal{M}$ that is a function of the solution $w(t)$ at the final time. A change in $\mathcal{S}$ then results in a change

$$\delta I = \frac{1}{T}\int_0^{t_f} \left(\frac{\partial \mathcal{L}^T}{\partial w}\delta w + \frac{\partial \mathcal{L}^T}{\partial \mathcal{S}}\delta \mathcal{S}\right)\mathrm{d}t + \frac{\partial \mathcal{M}^T}{\partial w}\delta w(t_f) \tag{10}$$

in the cost function. Using control theory, the governing equations of the flowfield are now introduced as a constraint in such a way that the final expression for the gradient does not require reevaluation of the flowfield. To achieve this, δw must be eliminated from Eq. (10). From Eq. (3), a variation of the semidiscrete form of the governing equations can be written as

$$V\frac{\partial}{\partial t}\delta w + \left[\frac{\partial R}{\partial w}\right]\delta w + \left[\frac{\partial R}{\partial \mathcal{S}}\right]\delta \mathcal{S} = 0$$

Next, introduce a Lagrange multiplier ψ to the time-dependent flow equation and integrate it over time to yield

$$\frac{1}{T}\int_0^{t_f} \psi^T\left(V\frac{\partial}{\partial t}\delta w + \left[\frac{\partial R}{\partial w}\right]\delta w + \left[\frac{\partial R}{\partial \mathcal{S}}\right]\delta \mathcal{S}\right) = 0 \tag{11}$$

Subtract Eq. (11) from the variation of the cost function to arrive at the following equation:

$$\begin{aligned}\delta I = {} & \frac{1}{T}\int_0^{t_f} \left(\frac{\partial \mathcal{L}^T}{\partial w}\delta w + \frac{\partial \mathcal{L}^T}{\partial \mathcal{S}}\delta \mathcal{S}\right)\mathrm{d}t + \frac{\partial \mathcal{M}^T}{\partial w}\delta w(t_f) \\ & - \frac{1}{T}\int_0^{t_f} \psi^T\left(V\frac{\partial}{\partial t}\delta w + \left[\frac{\partial R}{\partial w}\right]\delta w + \left[\frac{\partial R}{\partial \mathcal{S}}\right]\delta \mathcal{S}\right)\mathrm{d}t\end{aligned} \tag{12}$$

Next, collect the δw and $\delta \mathcal{S}$ terms and integrate

$$\frac{1}{T}\int_0^{t_f} \psi^T V\frac{\partial}{\partial t}\delta w\,\mathrm{d}t$$

by parts, to yield

$$\begin{aligned}\delta I = {} & \frac{1}{T}\int_0^{t_f} \left(\frac{\partial \mathcal{L}^T}{\partial w} + V\frac{\partial \psi^T}{\partial t} - \psi^T\left[\frac{\partial R}{\partial w}\right]\right)\delta w\,\mathrm{d}t \\ & + \left(\frac{\partial \mathcal{M}^T}{\partial w} - \frac{V}{T}\psi^T(t_f)\right)\delta w(t_f) + \frac{1}{T}\int_0^{t_f} \left(\frac{\partial \mathcal{L}^T}{\partial \mathcal{S}} - \psi^T\left[\frac{\partial R}{\partial \mathcal{S}}\right]\right)\delta \mathcal{S}\,\mathrm{d}t\end{aligned}$$

Choose ψ to satisfy the adjoint equation

$$V\frac{\partial \psi}{\partial t} - \left[\frac{\partial R}{\partial w}\right]^T\psi = -\frac{\partial \mathcal{L}}{\partial w}$$

with the terminal boundary condition

$$\frac{V}{T}\psi(t_f) = \frac{\partial \mathcal{M}}{\partial w}$$

Then the variation of the cost function reduces to

$$\delta I = \mathcal{G}^T\delta \mathcal{S}$$

where

$$\mathcal{G}^T = \frac{1}{T}\int_0^{t_f} \left(\frac{\partial \mathcal{L}^T}{\partial \mathcal{S}} - \psi^T\frac{\partial R}{\partial \mathcal{S}}\right)\mathrm{d}t$$

Optimal control of time-dependent trajectories is generally complicated by the need to solve the adjoint equation in reverse time from a final boundary condition using data from the trajectory solution, which in turn depends on the control derived from the adjoint solution. The sensitivities are determined by the solution of the adjoint equation in reverse time from the terminal boundary condition and the time-dependent solution of the flow equation. These sensitivities are then used to get a direction of improvement and steps are taken until convergence is achieved.

IV. Time-Accurate Continuous Adjoint Equation

To formulate the time-accurate continuous adjoint equation, we first introduce the cost function. In this work, the cost function is chosen to be the time-averaged drag coefficient and is defined as

$$\begin{aligned}I &= \frac{1}{T}\int_0^{t_f} C_d\,\mathrm{d}t = \frac{1}{T}\int_0^{t_f} C_a\cos\alpha + C_n\sin\alpha\,\mathrm{d}t \\ &= \frac{1}{\frac{1}{2}\gamma p_\infty M_\infty^2 \bar{c}T}\int_0^{t_f}\int_{\mathcal{B}} p\left(\frac{\partial x_2}{\partial \xi}\cos\alpha - \frac{\partial x_1}{\partial \xi}\sin\alpha\right)\mathrm{d}\xi\,\mathrm{d}t\end{aligned}$$

where C_a and C_n are the axial and normal force coefficients, respectively. The design problem is now treated as a control problem in which the control function is the airfoil shape, which is chosen to minimize I subject to the constraints defined by the flow equations. A variation in the shape causes a variation δp in the pressure and, consequently, a variation in the cost function:

$$\begin{aligned}\delta I = {} & \frac{1}{\frac{1}{2}\gamma p_\infty M_\infty^2 \bar{c}T}\int_0^{t_f}\int_{\mathcal{B}} \delta p\left[\frac{\partial x_2}{\partial \xi}\cos\alpha - \frac{\partial x_1}{\partial \xi}\sin\alpha\right] \\ & + p\left[\delta\left(\frac{\partial x_2}{\partial \xi}\right)\cos\alpha - \delta\left(\frac{\partial x_1}{\partial \xi}\right)\sin\alpha\right]\mathrm{d}\xi\,\mathrm{d}t\end{aligned} \tag{13}$$

Because p depends on w through the equation of state, then the variation δp is determined from the variation δw. From Eq. (2), the variation of the governing equation can be written as

$$V\frac{\partial}{\partial t}\delta w + \frac{\partial}{\partial \xi_i}\delta F_i = 0$$

where $\delta F_i = C_i\delta w + \delta S_{ij}f_j$. The Euler Jacobian matrix in the computational domain C_i is defined as $C_i = S_{ij}A_j$, where $A_i = \partial f_i/\partial w$ is the Euler Jacobian matrix. Multiplying by a costate vector ψ, also known as a Lagrange multiplier, and integrating over the space and time produces

$$\frac{1}{T}\int_0^{t_f}\int_{\mathcal{D}} \psi^T\left[V\frac{\partial}{\partial t}\delta w + \frac{\partial}{\partial \xi_i}(C_i\delta w + \delta S_{ij}f_j)\right]\mathrm{d}\mathcal{D}\,\mathrm{d}t = 0$$

If we confine the simulations to rigid mesh translation, then we can separate the equation into two terms and switch the order of the domain and time integrals for the first term, to yield

$$\begin{aligned}&\int_{\mathcal{D}}\frac{1}{T}\int_0^{t_f} \psi^T V\frac{\partial}{\partial t}\delta w\,\mathrm{d}t\,\mathrm{d}\mathcal{D} \\ &\quad + \frac{1}{T}\int_0^{t_f}\int_{\mathcal{D}} \psi^T\frac{\partial}{\partial \xi_i}(C_i\delta w + \delta S_{ij}f_j)\,\mathrm{d}\mathcal{D}\,\mathrm{d}t = 0\end{aligned}$$

If ψ is differentiable, then the two terms in the preceding equation can be integrated by parts, to give

$$\begin{aligned}&\int_{\mathcal{D}}\left(\frac{1}{T}[V\psi^T\delta w]_0^{t_f} - \frac{1}{T}\int_0^{t_f} V\frac{\partial \psi^T}{\partial t}\delta w\,\mathrm{d}t\right)\mathrm{d}\mathcal{D} \\ &\quad + \frac{1}{T}\int_0^{t_f}\left[\int_{\mathcal{B}} n_i\psi^T(C_i\delta w + \delta S_{ij}f_j)\,\mathrm{d}\mathcal{B}\right. \\ &\quad \left. - \int_{\mathcal{D}}\frac{\partial \psi^T}{\partial \xi_i}(C_i\delta w + \delta S_{ij}f_j)\,\mathrm{d}\mathcal{D}\right]\mathrm{d}t = 0\end{aligned}$$

The next procedure is to rearrange the terms in the equation such that

integrands that are multiplied by the variation of the state vector, δw, are grouped together and terms that are multiplied by the variation of the metric terms are separated into a different integral. This procedure is crucial to isolate the integral that will produce the time-accurate continuous adjoint equation:

$$\int_{\mathcal{D}} \frac{1}{T}[V\psi^T(t_f)\delta w(t_f) - V\psi^T(0)\delta w(0)]\,\mathrm{d}\mathcal{D} - \frac{1}{T}\int_0^{t_f}\int_{\mathcal{D}} V\frac{\partial \psi^T}{\partial t}\delta w + \frac{\partial \psi^T}{\partial \xi_i} C_i \delta w\,\mathrm{d}\mathcal{D}\,\mathrm{d}t + \frac{1}{T}\int_0^{t_f}\int_{\mathcal{B}} n_i\psi^T\delta F_i\,\mathrm{d}\mathcal{B} + \frac{1}{T}\int_0^{t_f}\left[\int_{\mathcal{B}} n_i\psi^T\delta S_{ij}f_j\,\mathrm{d}\mathcal{B} - \int_{\mathcal{D}}\frac{\partial\psi^T}{\partial\xi_i}\delta S_{ij}f_j\,\mathrm{d}\mathcal{D}\right]\mathrm{d}t = 0$$

Because the left-hand expression equals zero, it may be subtracted from the variation of the cost function (13) to give

$$\begin{aligned}\delta I = {} & \frac{1}{\frac{1}{2}\gamma p_\infty M_\infty^2 \bar{c} T}\int_0^{t_f}\int_{\mathcal{B}_w}\delta p\left[\frac{\partial x_2}{\partial\xi}\cos\alpha - \frac{\partial x_1}{\partial\xi}\sin\alpha\right] \\ & + p\left[\delta\left(\frac{\partial x_2}{\partial\xi}\right)\cos\alpha - \delta\left(\frac{\partial x_1}{\partial\xi}\right)\sin\alpha\right]\mathrm{d}\xi\,\mathrm{d}t \\ & - \int_{\mathcal{D}}\frac{1}{T}[V\psi^T(t_f)\delta w(t_f) - V\psi^T(0)\delta w(0)]\,\mathrm{d}\mathcal{D} \\ & + \frac{1}{T}\int_0^{t_f}\int_{\mathcal{D}}\left[V\frac{\partial\psi^T}{\partial t} + \frac{\partial\psi^T}{\partial\xi_i}C_i\right]\delta w\,\mathrm{d}\mathcal{D}\,\mathrm{d}t \\ & - \frac{1}{T}\int_0^{t_f}\int_{\mathcal{B}} n_i\psi^T\delta F_i\,\mathrm{d}\mathcal{B} - \frac{1}{T}\int_0^{t_f}\left[\int_{\mathcal{B}} n_i\psi^T\delta S_{ij}f_j\,\mathrm{d}\mathcal{B}\right. \\ & \left. - \int_{\mathcal{D}}\frac{\partial\psi^T}{\partial\xi_i}\delta S_{ij}f_j\,\mathrm{d}\mathcal{D}\right]\mathrm{d}t \end{aligned} \tag{14}$$

Because ψ is an arbitrary differentiable function, it may be chosen in such a way that δI no longer depends explicitly on the variation of the state vector, δw. The gradient of the cost function can then be evaluated directly from the metric variations without having to recompute the variation δw resulting from the perturbation of each design variable. The variation δw can then be eliminated by solving for the Lagrange multiplier ψ by setting the transpose of the integrand of the second integral in the third line of Eq. (14) to zero to produce a differential adjoint system governing ψ:

$$V\frac{\partial\psi}{\partial t} + C_i^T\frac{\partial\psi}{\partial\xi_i} = 0 \quad \text{in } \mathcal{D} \tag{15}$$

The convective flux of the time-accurate continuous adjoint equation (15) is discretized using a second-order central spatial discretization. The temporal discretization is based on a second-order backward-difference formula. Artificial dissipation based on the Jameson et al. [20] scheme, similar to that employed for the flow solver, is added to stabilize the scheme. Refer to Nadarajah [21] for a more detailed overview of the numerical discretization. A pseudotime derivative is added and the time-accurate adjoint equation is marched to a periodic steady-state solution.

At the outer boundary, incoming characteristics for ψ correspond to outgoing characteristics for δw. Consequently, we can choose boundary conditions for ψ such that

$$n_i\psi^T C_i\delta w = 0$$

If the coordinate transformation is such that δS is negligible in the far field, then the only remaining boundary term is

$$-\int_{\mathcal{B}_w}\psi^T\delta F_2\,\mathrm{d}\xi_1$$

Thus, by letting ψ satisfy the boundary condition, then

$$\psi_j n_j = \frac{1}{\frac{1}{2}\gamma p_\infty M_\infty^2\bar{c}}\left[\frac{\partial x_2}{\partial\xi}\cos\alpha - \frac{\partial x_1}{\partial\xi}\sin\alpha\right] \quad \text{on } \mathcal{B}_W \tag{16}$$

where n_j are the components of the surface normal. Because the initial condition for the Lagrange multipliers are set to zero, then $V\psi^T(0)\delta w(0) = 0$. If the problem is periodic in nature and the cost function used for this problem is not dependent upon t_f, then $V\psi^T(t_f)\delta w(t_f) = 0$. Equation (14) finally reduces to the following:

$$\begin{aligned}\delta I = {} & \frac{1}{\frac{1}{2}\gamma p_\infty M_\infty^2\bar{c}T}\int_0^{t_f}\int_{\mathcal{B}_w} p\left[\delta\left(\frac{\partial x_2}{\partial\xi}\right)\cos\alpha - \delta\left(\frac{\partial x_1}{\partial\xi}\right)\sin\alpha\right]\mathrm{d}\xi\,\mathrm{d}t \\ & - \frac{1}{T}\int_0^{t_f}\left[\int_{\mathcal{B}} n_i\psi^T\delta S_{ij}f_j\,\mathrm{d}\mathcal{B} - \int_{\mathcal{D}}\frac{\partial\psi^T}{\partial\xi_i}\delta S_{ij}f_j\,\mathrm{d}\mathcal{D}\right]\mathrm{d}t\end{aligned}$$

The preceding equation is then used to solve for the gradient, which can then provide a direction of improvement to reduce the objective function.

V. Time-Accurate Discrete Adjoint Equation

As in the case of steady flow, the time-accurate discrete adjoint equation is obtained by applying control theory directly to the set of time-accurate discrete field equations. The resulting equation depends on the type of scheme used to solve the flow equations. To formulate the discrete adjoint equation, we first take a variation of Eq. (8) with respect to w and $\mathcal{S}$ (only terms that are multiplied to δw are shown):

$$\delta R_{i,j}^{*^{n+1}}(w) = V_{i,j}\left[\frac{3}{2\Delta t}\delta w_{i,j}^{n+1} - \frac{2}{\Delta t}\delta w_{i,j}^{n} + \frac{1}{2\Delta t}\delta w_{i,j}^{n-1}\right] + \delta R_{i,j}^{n+1}(w) \tag{17}$$

Next, multiply the preceding equation by the transpose of the Lagrange multiplier and sum over the domain and time, to yield

$$\frac{1}{T}\sum_{t=0}^{t_f}\sum_{\Omega}\psi_{i,j}^T\delta R_{i,j}^* = \cdots + \frac{1}{T}[\psi_{i,j}^{T^{n+1}}\delta R_{i,j}^{*^{n+1}} + \psi_{i,j}^{T^{n+2}}\delta R_{i,j}^{*^{n+2}} + \psi_{i,j}^{T^{n+3}}\delta R_{i,j}^{*^{n+3}}] + \cdots \tag{18}$$

Substitute Eq. (17) into the $n+1$, $n+2$, and $n+3$ terms of the modified residual in the preceding equation, to yield

$$\begin{aligned}\frac{1}{T}\sum_{t=0}^{t_f}\sum_{\Omega}\psi_{i,j}^T\delta R_{i,j}^* = {} & \cdots + \frac{\psi_{i,j}^{T^{n+1}}}{T}V_{i,j}\left[\frac{3}{2\Delta t}\delta w_{i,j}^{n+1} - \frac{2}{\Delta t}\delta w_{i,j}^{n} + \frac{1}{2\Delta t}\delta w_{i,j}^{n-1} + \delta R_{i,j}^{n+1}\right] \\ & + \frac{\psi_{i,j}^{T^{n+2}}}{T}V_{i,j}\left[\frac{3}{2\Delta t}\delta w_{i,j}^{n+2} - \frac{2}{\Delta t}\delta w_{i,j}^{n+1} + \frac{1}{2\Delta t}\delta w_{i,j}^{n} + \delta R_{i,j}^{n+2}\right] \\ & + \frac{\psi_{i,j}^{T^{n+3}}}{T}V_{i,j}\left[\frac{3}{2\Delta t}\delta w_{i,j}^{n+3} - \frac{2}{\Delta t}\delta w_{i,j}^{n+2} + \frac{1}{2\Delta t}\delta w_{i,j}^{n+1} + \delta R_{i,j}^{n+3}\right] + \cdots\end{aligned}$$

Keeping only the $n+1$ terms, the preceding equation reduces to

$$\frac{1}{T}\sum_{t=0}^{t_f}\sum_{\Omega}\psi_{i,j}^T\delta R_{i,j}^* = \cdots + \frac{V_{i,j}}{T}\left[\frac{3}{2\Delta t}\psi_{i,j}^{T^{n+1}} - \frac{2}{\Delta t}\psi_{i,j}^{T^{n+2}} + \frac{1}{2\Delta t}\psi_{i,j}^{T^{n+3}}\right]\delta w_{i,j}^{n+1} + \frac{1}{T}\psi_{i,j}^{T^{n+1}}\delta R_{i,j}^{n+1} + \cdots \tag{19}$$

Next, we introduce the discrete cost function for the drag minimization problem as

$$\begin{aligned}I_c = {} & \frac{1}{T}\sum_{t=0}^{t_f} C_d\Delta t = \frac{1}{T}\sum_{t=0}^{t_f}(C_a\cos\alpha + C_n\sin\alpha)\Delta t \\ = {} & \frac{1}{\frac{1}{2}\gamma p_\infty M_\infty^2\bar{c}T}\sum_{t=0}^{t_f}\sum_{i=\mathrm{LTE}}^{\mathrm{UTE}} p_{i,W}(\Delta x_{2\xi i}\cos\alpha - \Delta x_{1\xi i}\sin\alpha)\Delta t\end{aligned}$$

where LTE is the lower trailing edge, UTE is the upper trailing edge,

and $p_{i,W}$ is the wall pressure. In this research, the wall pressure is defined as

$$p_{i,W} = \frac{1}{2}(p_{i,2} + p_{i,1})$$

where $p_{i,2}$ and $p_{i,1}$ are the values of the pressure in the cell above and below the wall. A variation in the cost function will result in a variation Δp in the pressure and variations $\Delta x_{2\xi}$ and $\Delta x_{1\xi}$ in the metrics. The variation of the cost function for drag minimization can be written as

$$\begin{aligned}\delta I_c = &\frac{1}{\frac{1}{2}\gamma p_\infty M_\infty^2 \bar{c} T} \\ &\times \sum_{t=0}^{t_f}\Bigg[\sum_{i=\mathrm{LTE}}^{\mathrm{UTE}} \frac{1}{2}(\Delta x_{2\xi i}\cos\alpha - \Delta x_{1\xi i}\sin\alpha)\frac{\partial p}{\partial w}(\delta w_{i,2} + \delta w_{i,1}) \\ &+ \sum_{i=\mathrm{LTE}}^{\mathrm{UTE}}\left(\frac{1}{2}(p_{i,2} + p_{i,1}) - p_\infty\right)[\cos\alpha\delta(\Delta x_{2\xi i}) \\ &- \sin\alpha\delta(\Delta x_{1\xi i})]\Bigg]\Delta t \end{aligned} \tag{20}$$

The time-dependent discrete Euler equations can now be introduced into δI as a constraint, to produce

$$\delta I = \delta I_c - \frac{1}{T}\sum_{t=0}^{t_f}\sum_{\Omega}\psi_{i,j}^T \delta R_{i,j}^*(w) \tag{21}$$

Substitute Eqs. (19) and (20) into the preceding expression, which can then be rearranged into two main categories: first, terms that are multiplied by the variation of the state vector, δw; second, terms that are multiplied by the variation of the shape function, $\delta\mathcal{S}$. The time-accurate discrete adjoint equation can now be defined as

$$\begin{aligned}&\frac{\partial \psi_{i,j}^{n+1}}{\partial\tau} - V_{i,j}\left[\frac{3}{2\Delta t}\psi_{i,j}^{T^{n+1}} - \frac{2}{\Delta t}\psi_{i,j}^{T^{n+2}} + \frac{1}{2\Delta t}\psi_{i,j}^{T^{n+3}}\right] \\ &- \psi_{i,j}^{T^{n+1}}\delta_w R_{i,j}^{n+1} = 0\end{aligned} \tag{22}$$

The first term, $\partial\psi_{i,j}^{n+1}/\partial\tau$, is added to march the solution in a fictitious time τ to a periodic steady-state solution. The second term represents a second-order forward-difference formula for the temporal discretization of the time-accurate adjoint equation. The term demonstrates that to acquire the solution of the adjoint equation at the time step $n+1$ requires the solution at $n+2$ and $n+3$. Therefore, the adjoint equation is integrated backward in time from a terminal boundary condition. The last term requires the variation of the residual as a function of the state vector. Here, $R_{i,j}^{n+1}$ denotes the discrete representation of the residual which is the sum of the discrete convective and dissipative fluxes in each cell. A full differentiation of the equation would involve differentiating every term that is a function of w. A collection of all terms that are multiplied to δw will produce the discrete adjoint convective and dissipative fluxes. Refer to Nadarajah [21] for a complete derivation of the discrete adjoint fluxes.

To acquire the discrete adjoint boundary condition, Eq. (22) can be expanded at cell $i, 2$ to create the following:

$$\begin{aligned}&\frac{\partial \psi_{i,2}^{n+1}}{\partial\tau} - V_{i,2}\left[\frac{3}{2\Delta t}\psi_{i,2}^{T^{n+1}} - \frac{2}{\Delta t}\psi_{i,2}^{T^{n+2}} + \frac{1}{2\Delta t}\psi_{i,2}^{T^{n+3}}\right] \\ &-\frac{1}{2}\Big[A_{i-\frac{1}{2},2}^{T^{n+1}}\left(\psi_{i,2}^{n+1} - \psi_{i-1,2}^{n+1}\right) + A_{i+\frac{1}{2},2}^{T^{n+1}}\left(\psi_{i+1,2}^{n+1} - \psi_{i,2}^{n+1}\right) \\ &+ B_{i,\frac{5}{2}}^{T^{n+1}}\left(\psi_{i,3}^{n+1} - \psi_{i,2}^{n+1}\right) - \Phi\Big] = 0\end{aligned} \tag{23}$$

where A and B are the Euler Jacobians in the ξ and η directions, and Φ is the source term for drag minimization,

$$\begin{aligned}\Phi = &\Delta x_{2\xi i}\psi_{2_{i,2}}^{n+1} - \Delta x_{1\xi i}\psi_{3_{i,2}}^{n+1} + \Big(\Delta x_{2\xi i}\omega\cos\alpha \\ &- \Delta x_{1\xi i}\omega\sin\alpha\Big)\frac{\partial p}{\partial w}\Delta t\end{aligned}$$

All of the terms in Eq. (23), except for the source term, scale as the square of Δx_i. Therefore, as the mesh width is reduced, the terms in the source term must approach zero as the solution reaches a steady state. One then recovers the continuous adjoint boundary condition, as stated in Eq. (16). Equation (21) then simplifies to the following form:

$$\begin{aligned}\delta I = \cdots + \frac{1}{T}\Bigg[&\left(\frac{1}{2}(p_{i,2} + p_{i,1}) - p_\infty\right)[\delta(\Delta x_{2\xi i})\omega\cos\alpha \\ &- \delta\Big(\Delta x_{1\xi i})\omega\sin\alpha]\Delta t - \psi_{i,j}^{T^{n+1}}\delta_f R_{i,j}^{n+1}\Bigg] + \cdots\end{aligned}$$

The preceding equation represents the total gradient obtained using the time-accurate discrete adjoint approach to reduce the total drag of a pitching airfoil, and $\delta_f R_{i,j}^{n+1}$ represents the variation of the residual as a function of the shape function.

VI. Design Process

The objective of this work is to change the shape of the airfoil to minimize its time-averaged coefficient of drag. Given the derivation provided in previous sections, the adjoint boundary condition can easily be modified to admit other figures of merit. The shape of the airfoil is constrained such that the maximum thickness-to-chord ratio remains constant between the initial and final designs. In addition, the mean angle of attack α_o is allowed to vary to ensure that the time-averaged coefficient of lift remains constant between designs. The airfoil undergoes a forced pitching oscillation about the quarter-chord. The angle of incidence is given by

$$\alpha(t) = \alpha_o + \alpha_m \sin(\omega t)$$

where $\alpha_o = 0$ deg, and the maximum angle of attack is $\alpha_m = 1.01$ deg. One period of oscillation is defined from $t = 0$ to $t = 2\pi$. To compute the entire unsteady flow solution for each period, $\alpha(t)$ is divided into N discrete points or time steps. The individual steps within each iteration of the design process for the full unsteady design and multipoint approaches are outlined next.

A. Full Unsteady Design

The following steps detail the procedures for the full unsteady continuous and discrete adjoint-based design optimization problem:

1. *Unsteady Flow Calculation*

A multigrid scheme is used to drive the unsteady residual at each time step to a negligible value. The duration of the physical time history (typically quantified in the number of oscillatory periods) depends on the physics of the flowfield and the accuracy requirements of the calculation. Generally, it requires five periods before a limit cycle is achieved. Here, a period refers to one full oscillation. During the last period, the flow solution at each time step is saved in memory. Fifteen multigrid cycles were used for each time step. If 24 time steps are used for each cycle and five cycles are used to achieve the limit cycle, then a total of 1800 multigrid cycles are required to obtain the unsteady solution. To maintain the time-averaged lift coefficient, the mean angle of attack α_o is perturbed. However, α_o is only modified every three periods, because it requires at least three periods for the global coefficients such as time-averaged lift and drag to converge to an accuracy level of 1E-3. A total of 15 periods are needed instead of five to achieve the desired time-averaged lift coefficient. This multiplies the total cost by three times.

2. *Unsteady Adjoint Calculation*

The unsteady adjoint equation, either the discrete or continuous version, requires integration in reverse time. The same numerical

scheme employed to solve the unsteady flow is used here, as well with minor adjustments in the code to allow integration in reverse time. Only three periods are needed before the limit cycle is achieved. Fifteen multigrid cycles are used at each time step, which translates to a total of 1080 cycles to achieve a limit cycle for the adjoint equation.

3. Gradient Evaluation

An integral over the last period of the adjoint solution is used to form the gradient. This gradient is then smoothed using an implicit smoothing technique. This ensures that each new shape in the optimization sequence remains smooth and acts as a preconditioner, which allows the use of much larger steps. The smoothing leads to a large reduction in the number of design iterations needed for convergence. Refer to Nadarajah and Jameson [22] for a more comprehensive overview of the gradient smoothing technique. An assessment of alternative search methods for a model problem is given by Jameson and Vassberg [23].

4. Airfoil-Shape Modification

The airfoil shape is then modified in the direction of improvement using a steepest-descent method.

Let $\mathcal{F}$ represent the design variable and $\mathcal{G}$ the gradient. An improvement can then be made with a shape change

$$\delta\mathcal{F} = -\lambda\mathcal{G}$$

where λ is determined by trial and error to ensure a fast rate of convergence while guaranteeing that the objective function convergence to an error level of at least 1E-6. The step-size value is constant for all cases presented in this work.

5. Grid Modification

The internal grid is modified based on perturbations on the surface of the airfoil. The method modifies the grid points along each grid index line projecting from the surface. The arc length between the surface point and the far-field point along the grid line is first computed, then the grid point at each location along the grid line is attenuated proportional to the ratio of its arc length distance from the surface point and the total arc length between the surface and the far field.

6. Repeat Design Process

The entire design process is repeated until the objective function converges. The problems in this work typically required between 9 and 25 design cycles. Each design cycle required 1800 multigrid cycles to compute the flow solution and 1080 cycles for the adjoint solution.

B. Multipoint Design

In the multipoint design approach, the unsteady flow and adjoint solvers are replaced with a steady flow and adjoint solver at each time step. The gradient is an average of the gradients from each time step, defined as

$$\bar{g} = \frac{1}{N}\sum_{i=1}^{N} \omega_{ti} g_i$$

where g_i is the gradient and ω_{ti} is the weight at each design point. In this work, the weights are chosen to be unity. If the time-averaged lift is not constrained, then only one period is required for both the flow and adjoint solvers, and the total computational cost is 720 multigrid cycles.

Table 1 Comparison of computational cost between the design approaches

Method	Euler (multigrid cycles)	Adjoint (multigrid cycles)	Cost
Multipoint	360	360	1
Full unsteady	1800	1080	4

Table 1 illustrates a cost comparison between the unsteady and multipoint design approaches. Here, the middle two columns contain the total number of multigrid cycles used to compute the Euler and adjoint equations. The numbers in the last column signify the ratio of cost of the unsteady design method with respect to the multipoint approach. Using the full unsteady design approach requires four times the computational cost as doing the multipoint approach. However, if the time-averaged lift is constrained, an additional four periods are required for the multipoint approach to converge the time-averaged lift coefficient and an additional ten are needed for the unsteady case. This brings the total number of multigrid cycles required by the flow solver per design cycle to 1800 for the multipoint case and 5400 for the unsteady. The cost of the adjoint solver remains the same, because the mean angle of attack is only modified during the flow-solver stage. The unsteady approach is then three times the computational cost of the multipoint approach.

The difference in cost between one steady Runge–Kutta iteration and one unsteady Runge–Kutta iteration was not factored into the computing cost, because the difference is minimal, requiring only the addition of the time derivatives of the flow variables for the implicit time-stepping algorithm.

VII. Results

The following subsections present results of the time-averaged drag minimization problem for a two-dimensional airfoil undergoing a periodic pitching motion. The first subsection contains a code-validation study. The second subsection is dedicated to a temporal-resolution study. The third subsection demonstrates the redesign of the RAE 2822 airfoil to reduce the time-averaged drag coefficient while maintaining the time-averaged lift. The last subsection presents a comparison between the multipoint and unsteady design approaches.

A. Code Validation

An Euler solution is computed on a 193×33 grid and the lift coefficient versus angle of attack is compared with the experimental NACA 64A010 CT6 [24] data. A spatial-resolution study [21] was conducted for grids of various types and sizes to determine the minimum number of grid points needed to establish an accurate hysteresis loop. It was deemed that a 193×33 grid, as shown in Fig. 1, was adequate for inviscid solutions.

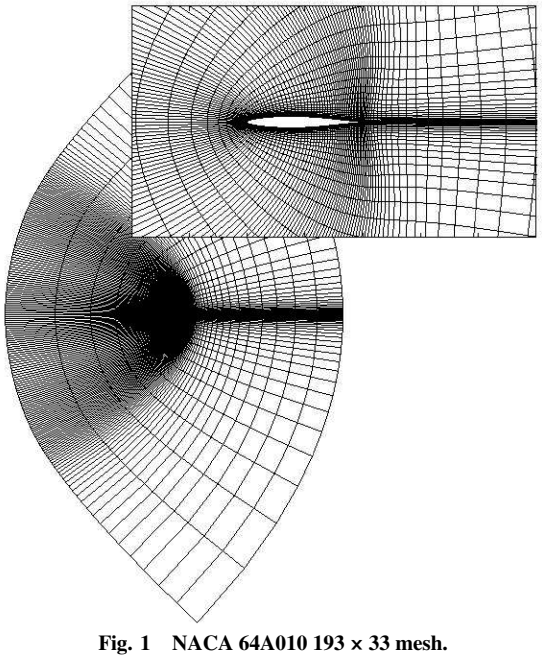

Fig. 1 NACA 64A010 193 × 33 mesh.

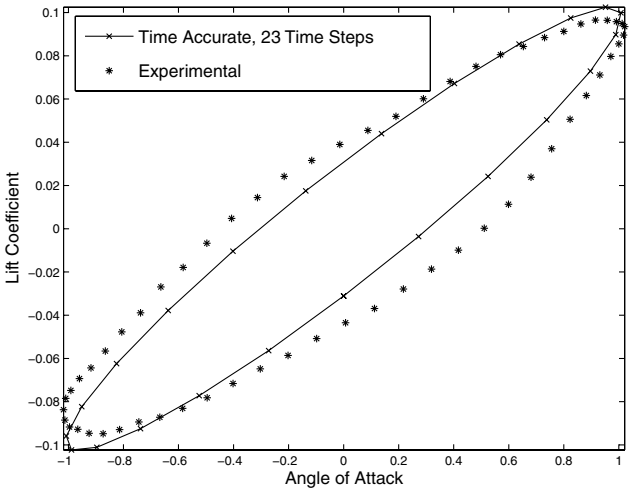

Fig. 2 Comparison of lift hysteresis with NACA 64A010 CT6 [24] experimental data at $M_\infty = 0.78$ and $\omega_r = 0.202$.

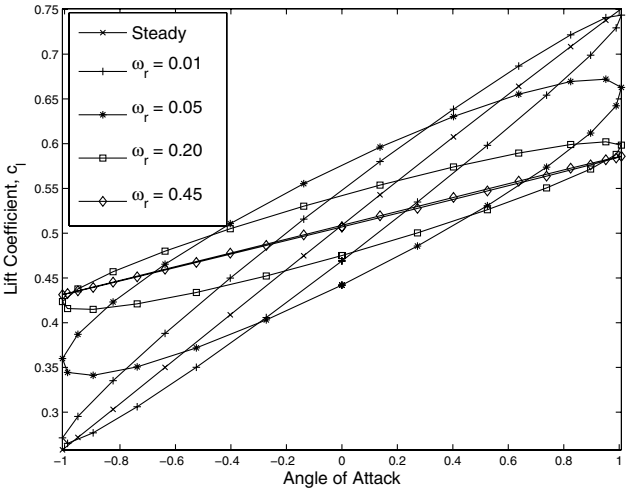

Fig. 4 Lift hysteresis at various reduced frequencies for the RAE 2822 at $M_\infty = 0.78$.

The computations are performed at a freestream Mach number of 0.78, a mean angle of attack of $\alpha_o = 0$ deg, a maximum angle of attack of $\alpha_m = 1.01$ deg, and at a reduced frequency of $\omega_r = 0.202$. Five periods of computation are required in order for the periodic flow to be established and to allow the time-averaged lift and drag coefficients to converge to an error level of 1E-3. Figure 2 illustrates the hysteresis loop and the results reproduce the experimental results with sufficient accuracy. In Fig. 2, the lift coefficient versus angle of attack loop moves in a counterclockwise direction. The nonlinear behavior due to the movement of the shock causes an amplitude reduction of the lift coefficient and a phase lag.

The primary goal of this work is to investigate the benefits of aerodynamic shape optimization of airfoils undergoing unsteady motion via an adjoint-based unsteady optimization approach. The traditional approach is to perform a multipoint design using solutions from various phases of the unsteady motion. The following subsections will establish that under specific conditions, there is an advantage to an unsteady optimization approach. First, a temporal-resolution study will be examined. Second, an optimization of a pitching airfoil to reduce drag will be demonstrated. Finally, a thorough investigation of the advantage of an unsteady optimization approach over a multipoint will be presented.

The chosen test case is that of a pitching RAE 2822 airfoil in transonic flow at a Mach number of 0.78, a mean angle of attack of $\alpha_o = 0$ deg, and a reduced frequency of $\omega_r = 0.20$ on a 193×33 grid. Figure 3 illustrates the convergence history for the unsteady flow solver and the unsteady continuous and discrete adjoint equations. The continuous and discrete unsteady adjoint equations have the same convergence rate, and the residuals reach machine zero within 100 multigrid W-cycles.

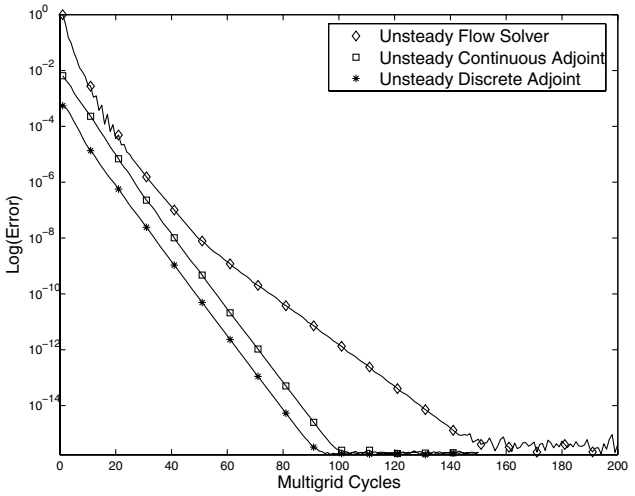

Fig. 3 Convergence history of the unsteady flow solver and unsteady continuous and discrete adjoint equations; 193 × 33 mesh; RAE 2822 airfoil at $M_\infty = 0.78$.

For unsteady transonic flows, as the airfoil oscillates at a small angle of attack, the shock wave moves back and forth about a mean location and is closely sinusoidal and lags the airfoil motion. This lag is evident in the lift hysteresis loop, in which the maximum lift does not occur at the maximum angle of attack. The nonlinear behavior of inviscid unsteady transonic flows is primarily due to the movement of the shock. According to McCroskey [25], however, the shock wave motion is greatest at moderate reduced frequencies. He further clarifies that for small-amplitude oscillations for reduced frequencies approximately below 0.5, large shock motion is seen. This motion gradually reduces as the reduced frequency increases. It is also expected that at very low reduced frequencies, the flow characteristics are very similar to that of steady-state computations. Lift hysteresis loops were computed for several different reduced frequencies at the same Mach number and are compared with the steady lift curve in Fig. 4. As expected, at a reduced frequency of 0.01, the lift-curve slope is similar to the steady solution and the slope reduces as the reduced frequency increases.

B. Temporal Resolution

To quantify the required number of time steps per period, a temporal convergence study was performed. The code was run with 5, 11, 23, 47, 95, and 191 time steps per period. At each time step, the modified residual $R^*(w_{i,j})$ from Eq. (8) was driven to machine zero.

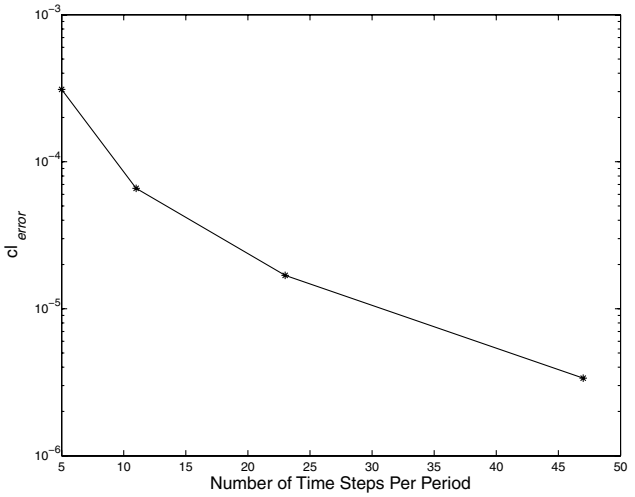

Fig. 5 $C_{l_{\text{error}}}$ as a function of the number of time steps per period using a logarithmic vertical scale.

Table 2 Time-averaged coefficient of lift as a function of temporal resolution

Time steps per period	5	11	23	47	95	191
C_l	0.5084	0.5086	0.5087	0.5087	0.5087	0.5087

To guarantee temporal convergence, both the time-averaged lift and drag coefficients were monitored. Generally, 60 time periods were needed to eliminate errors due to initial transients and to ensure a machine-zero convergence of the time-averaged lift and drag. Figure 5 illustrates the $C_{l_{\text{error}}}$ as a function of the temporal resolution. The case with 191 time steps per period was used as the control solution, and each point on the figure represents the difference between the time-averaged lift coefficient of the control solution and the current solution. Figure 5 illustrates that the error decay rate is proportional to Δt^2. Table 2 shows that 23 time steps per period is sufficient to obtain a lift coefficient accurate to four decimal places.

To perform optimum shape design for unsteady flows, it is important to access the required temporal resolution to obtain accurate sensitivity of the objective function to the design variable. In this work, the objective function is the time-averaged drag coefficient, and the design variables are the points on the surface of the airfoil. Figure 6 illustrates the L^2-norm of the gradient error as a function of temporal resolution for both the continuous and discrete adjoint approaches, using the gradient computed with 191 time steps as the control solution. The gradients of the two adjoint approaches converge at the same rate. To ensure accurate gradients, the residuals at each time step for both the flow and adjoint solvers were driven to machine zero, and 60 time periods were used for both solvers to ensure elimination of transient errors. The decay rate of the L^2-norm of the gradient error is proportional to Δt^2. The equivalent convergence decay rates between the gradient (Fig. 6) and time-averaged lift (Fig. 5) confirm the proper implementation of both the continuous and discrete adjoint equations. Figure 7 shows the gradient at each point on the surface of the airfoil. The figure illustrates that the gradient is almost identical to engineering accuracy for a vast range of points, except in the region of the shock wave between grid points 80 and 100. A closer inspection of the data reveals that these points converge as the temporal resolution is increased. This is further illustrated in Table 3, which shows the convergence of the L^2-norm of the gradient error. The gradient error for the case with 23 time steps per period is approximately 1e-04, providing an equivalent level of accuracy to that observed for the time-averaged lift. Thus, 23 time steps per period is deemed sufficient for this particular test case.

Figure 8 shows a comparison of the discrete and continuous adjoint gradients for the case with 23 time steps per period. A closer

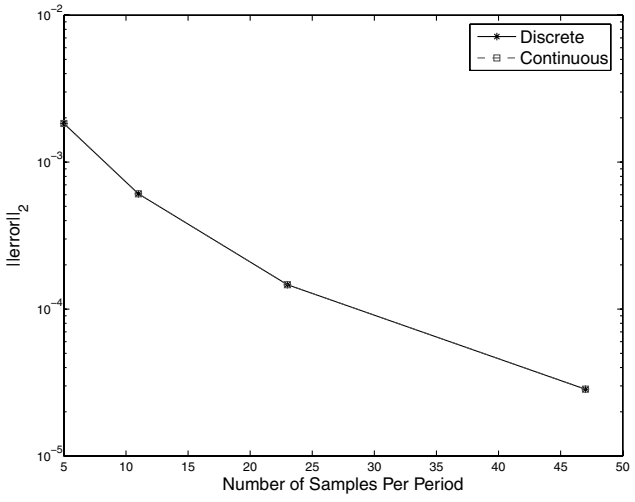

Fig. 6 Gradient error L^2-norm as a function of the number of time steps per period using a logarithmic vertical scale.

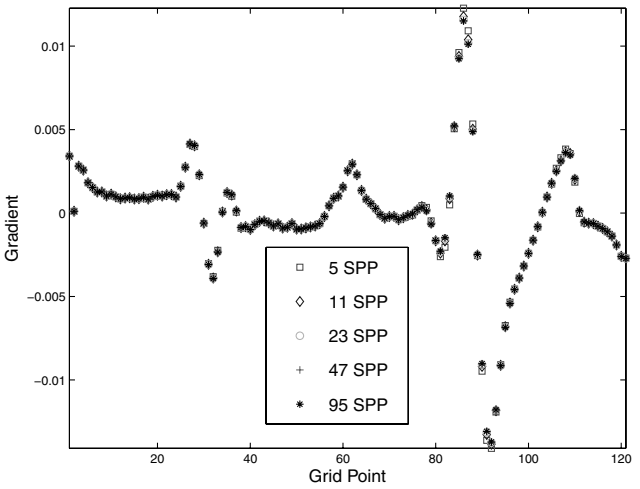

Fig. 7 Comparison of discrete unsteady adjoint gradients for various temporal resolutions.

examination of the discrete and continuous adjoint solutions reveals that the excellent gradient comparison is primarily due to the comparable adjoint solutions between the two approaches. A comparison of the second adjoint variable along the wall is demonstrated in Fig. 9. In Fig. 10, both the second and third adjoint variables are shown. Values are plotted for points along a grid line extending from the airfoil surface to the far-field boundary. The two methods differ in the manner that the adjoint convective and dissipative fluxes are discretized, as well as in the enforcement of the boundary condition. In the case of the continuous adjoint approach, the boundary condition is computed for the cells below the wall along $j = 1$; however, in the case of the discrete adjoint method, the boundary condition appears as source terms added to the adjoint convective and dissipative fluxes along the cells above the wall ($j = 2$). Therefore, the discrete adjoint approach does not require values of adjoint variables along $j = 1$; however, they are set to be equal to the values in $j = 2$. The effect of this difference in the enforcement of the boundary condition can be observed in a close-up view of the adjoint values close to the boundary, as illustrated in Fig. 10. Despite the difference in the boundary conditions and the slight difference in the adjoint solution, the two approaches produce virtually indistinguishable gradients, as demonstrated in Fig. 8.

C. Time-Averaged Drag Minimization of RAE 2822 Airfoil with Fixed Time-Averaged Lift Coefficient

Figure 11 illustrates the initial and final geometry for the RAE 2822 airfoil. The solid line represents the initial airfoil geometry and the dashed line illustrates the redesigned airfoil. A distinctive feature of the new airfoil is in the drastic reduction of the upper-surface curvature. A reduced curvature leads to a weaker shock and thus a lower wave drag, but it also leads to a reduction in airfoil camber, resulting in a loss in lift.

To maintain the time-averaged lift coefficient C_l, the mean angle of attack α_o is perturbed to a new value. The impact of this decision resulted in a need to compute more periods to allow the C_l and C_d to converge. In this work, α_o was perturbed every three periods. This allowed the C_l to converge to a new value before the angle of attack

Table 3 L^2-norm of the gradient error as a function of temporal resolution

Time steps per period	L^2-norm
5	1.8686e-03
11	6.1302e-04
23	1.4652e-04
47	2.8524e-05

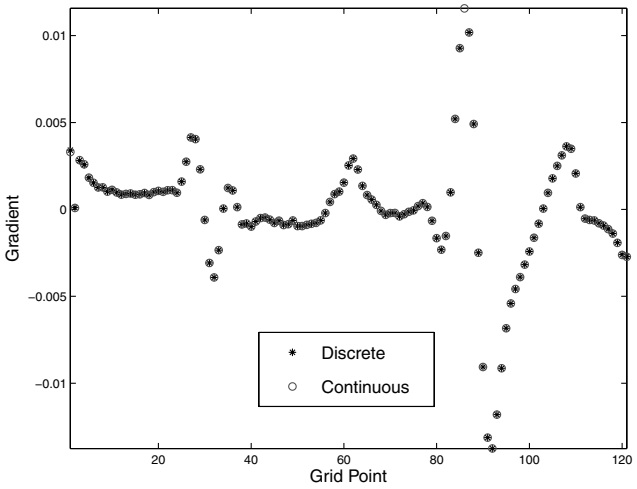

Fig. 8 Comparison of discrete and continuous unsteady adjoint gradients for 23 time steps per period.

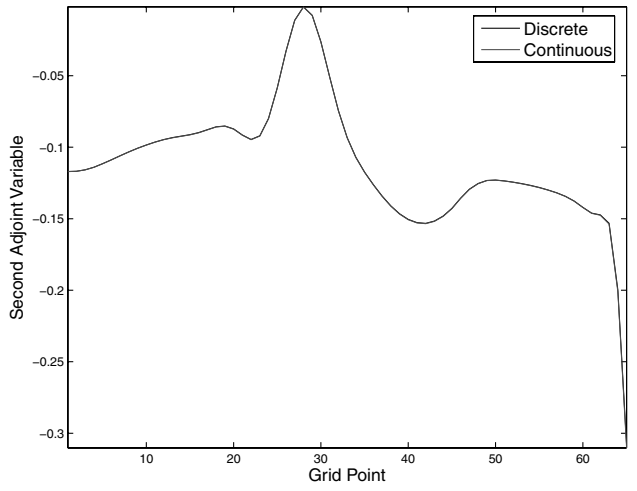

Fig. 9 Comparison of the second adjoint variable at the wall for the discrete and continuous unsteady adjoint methods for 23 time steps per period.

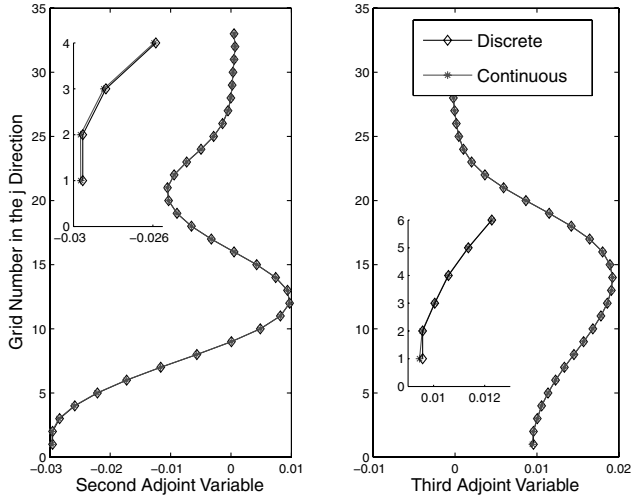

Fig. 10 Comparison of the second and third adjoint variables for the discrete and continuous unsteady adjoint methods for 23 time steps per period.

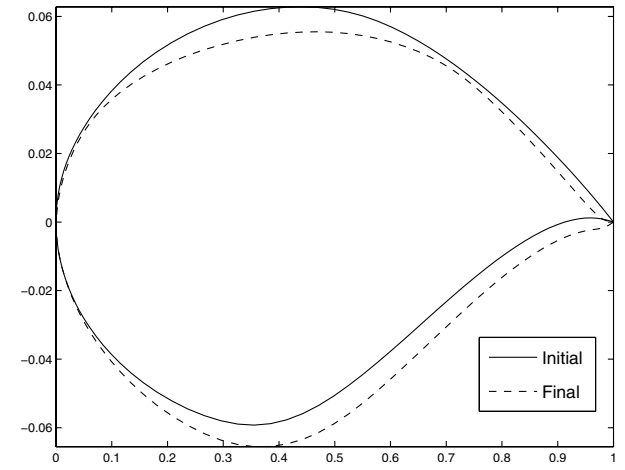

Fig. 11 Initial and final geometries for the RAE 2822 airfoil at $M_\infty = 0.78$, $\omega_r = 0.20$, and $\alpha_o = 0\,\text{deg}$.

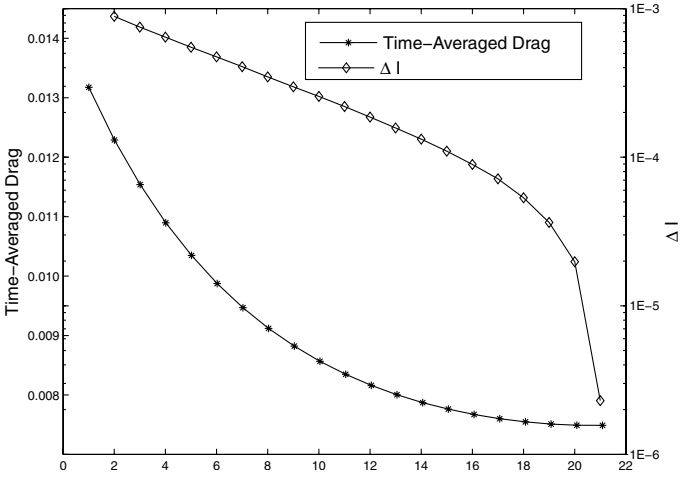

Fig. 12 Convergence of the time-averaged drag coefficient for the RAE 2822 airfoil at $M_\infty = 0.78$, $\omega_r = 0.20$, and $\alpha_o = 0\,\text{deg}$.

was perturbed any further. A total of 15 periods were used for each design cycle. Figure 12 illustrates the convergence rate of C_d, which is reduced by 43% from 132 drag counts to 75 drag counts within 21 design cycles. In Fig. 12, the change in the objective function or ΔI, where I is the objective function, is also shown. During the first 16 design cycles, ΔI converges linearly, as expected. Linear convergence is characteristic of a steepest-descent-type method. As the final airfoil profile is realized, the convergence ΔI increases rapidly. The code is automatically stopped as soon as a change of 1E-6 is detected. This level of change corresponds to a change to the sixth decimal place of the drag coefficient and this is sufficient for engineering accuracy.

Figure 13 illustrates the initial and final pressure contours at a 180-deg phase. The sonic line represented by a dashed line is overplotted on each figure. It is clearly visible that the strong shock on the upper surface of the initial geometry was considerably reduced. Figures 14a–14d illustrate the upper and lower surface instantaneous pressure coefficients for the initial and final design. In Fig. 14a, a comparison of the initial instantaneous pressure distribution versus the final at a 0-deg phase shows an almost complete reduction of the wave drag. The strong shock on the suction side of the airfoil is weakened at all other phases of the oscillation.

D. Multipoint Versus Unsteady Optimization

A multipoint design approach was often the method of choice for optimization of airfoils in an unsteady flow environment, due to its

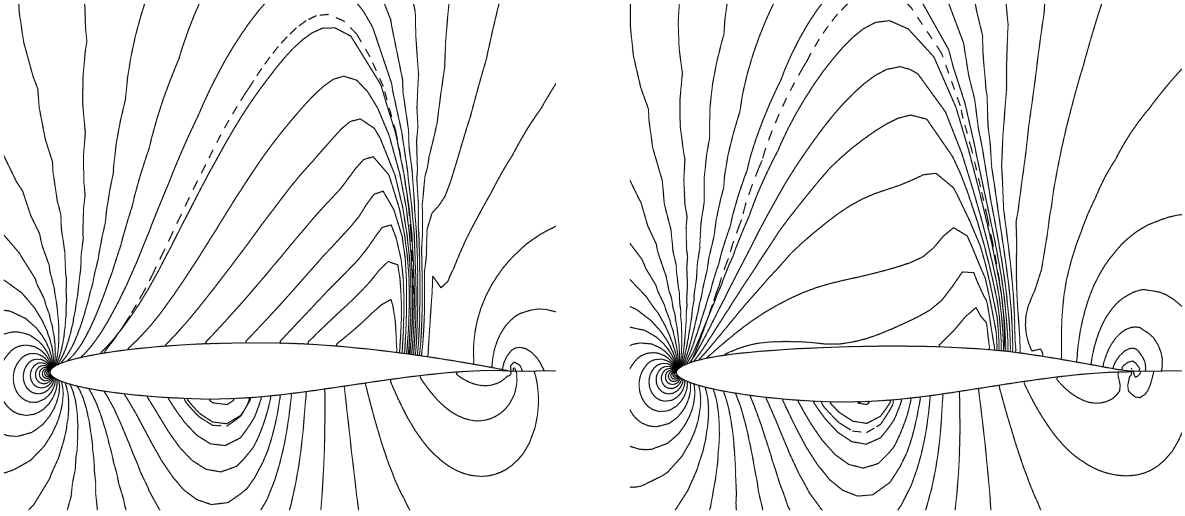

a) Initial airfoil, phase=180 deg **b) Final design, phase=180 deg**

Fig. 13 Pressure contour plot for the RAE 2822 airfoil at grid of 192 × 32, $M_\infty = 0.78$, $\omega_r = 0.20$, and fixed $C_l = 0.51$.

lower computational and memory cost. In this subsection of the paper, we make the argument that even if a multipoint design approach is cheaper, it cannot replace a full unsteady optimization technique. Through the use of final airfoil profiles, convergence histories, and gradient comparisons, the following results show that there are benefits to unsteady optimization.

To compare the unsteady optimization approach to that of the multipoint technique, unsteady design cases are computed at reduced

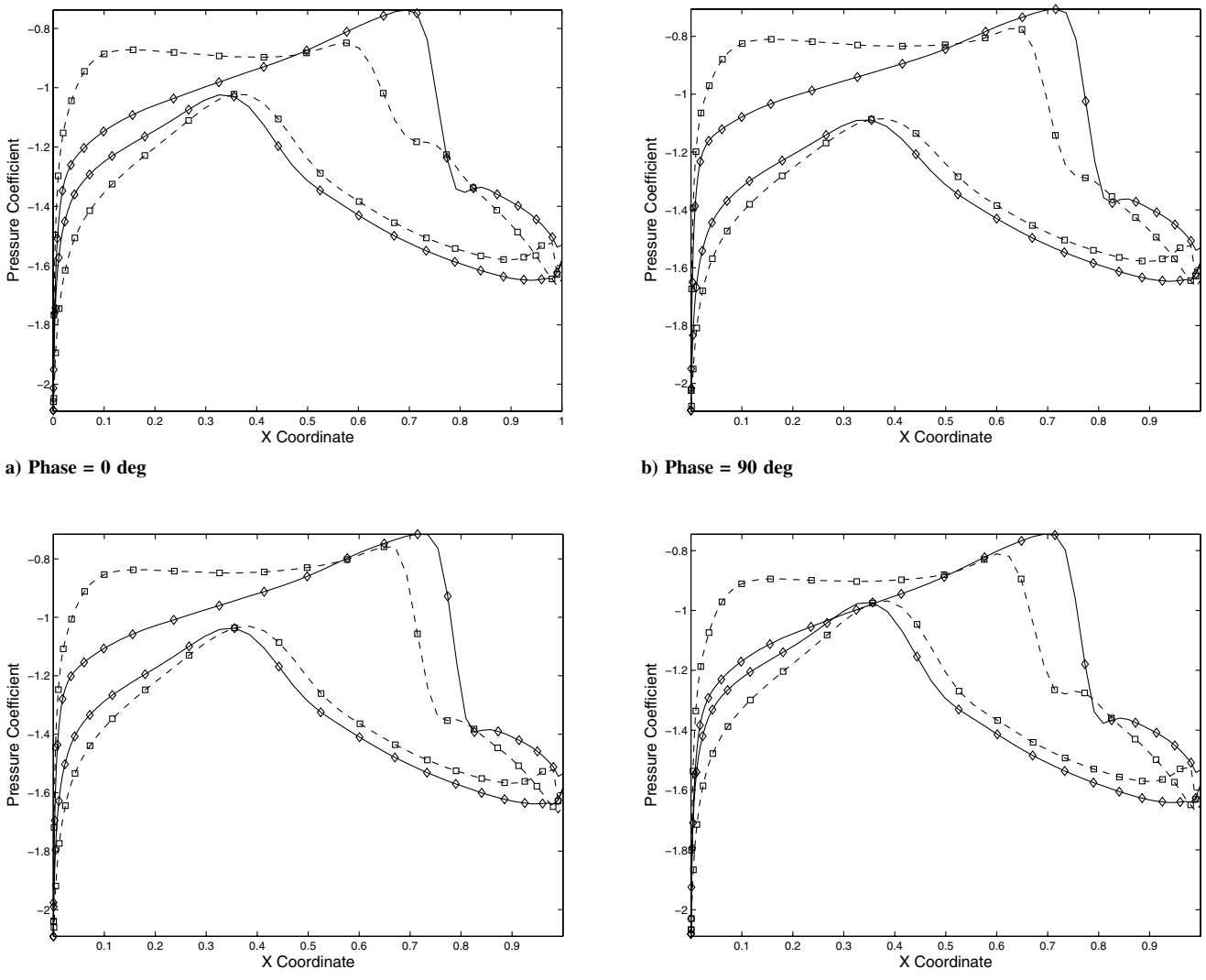

a) Phase = 0 deg **b) Phase = 90 deg**

c) Phase = 180 deg **d) Phase = 270 deg**

Fig. 14 Initial and final pressure coefficients at various phases for the RAE 2822 airfoil at $M_\infty = 0.78$, $\omega_r = 0.20$, and $\alpha_o = 0$ deg ($\diamond$ is initial pressure and $\square$ is final pressure).

frequencies ranging from 0.01 to 0.45 at a Mach number of $M_\infty = 0.78$. The time-averaged lift coefficient for all reduced frequencies is fixed at $C_l = 0.51$. Lift hysteresis loops for the various reduced frequencies are compared with the steady lift curve in Fig. 4.

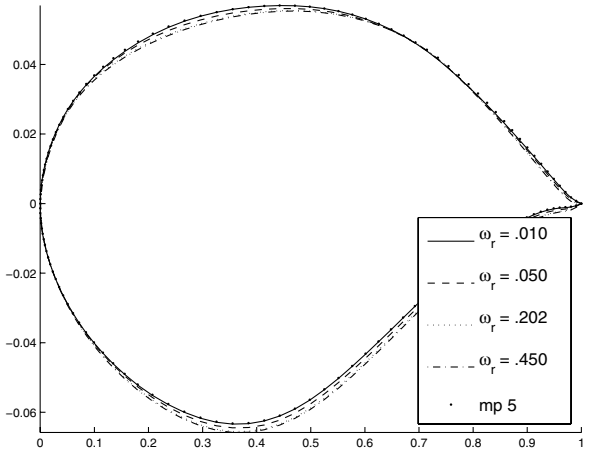

Fig. 15 Comparison of final airfoil geometries between various reduced frequencies and the multipoint approach at $M_\infty = 0.78$, $\bar{\alpha} = 0$ deg, and fixed $C_l = 0.51$.

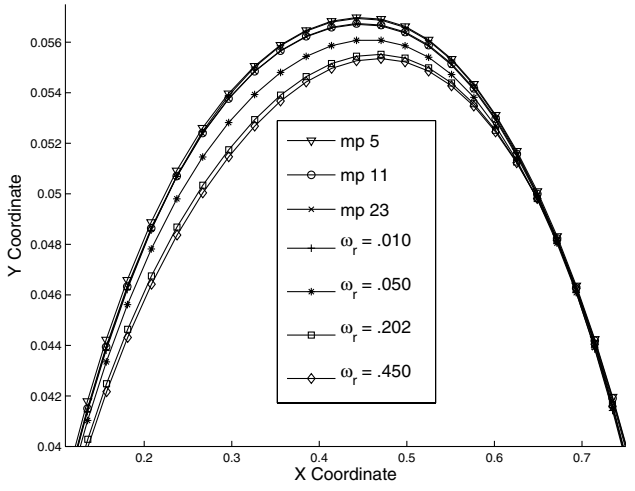

Fig. 16 Close-up view of the final airfoil geometry at $M_\infty = 0.78$, $\bar{\alpha} = 0$ deg, and fixed $C_l = 0.51$.

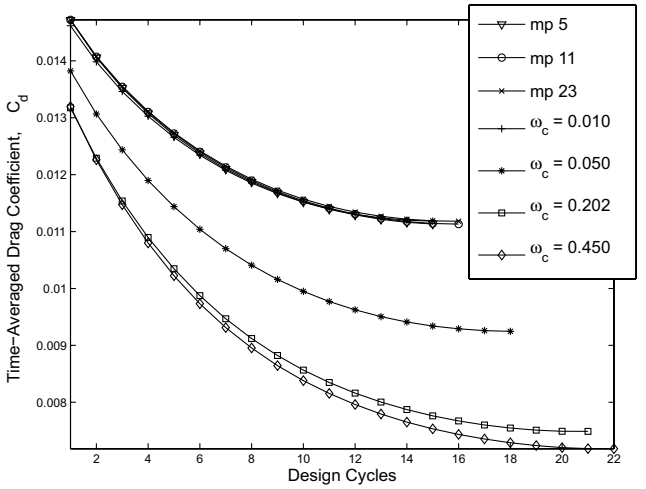

Fig. 17 Convergence history of the time-averaged drag coefficient for various design approaches for the RAE 2822 airfoil at $M_\infty = 0.78$, $\alpha_o = 0$ deg, and fixed $C_l = 0.51$.

Table 4 Initial and final time-averaged drag for various design approaches

Case	Initial C_d	Final C_d	Reduction
Multipoint, mp 5	0.0147	0.0111	24.5%
Multipoint, mp 11	0.0147	0.0111	24.5%
Multipoint, mp 23	0.0147	0.0112	23.8%
Full unsteady, $\omega_r = 0.01$	0.0146	0.0112	23.3%
Full unsteady, $\omega_r = 0.05$	0.0138	0.0092	33.3%
Full unsteady, $\omega_r = 0.20$	0.0132	0.0075	43.2%
Full unsteady, $\omega_r = 0.45$	0.0132	0.0072	45.5%

Figure 15 illustrates a comparison of final airfoil geometries between airfoils designed using the full unsteady optimization approach at various reduced frequencies and the multipoint technique. The airfoils are designed at a Mach number of $M_\infty = 0.78$, a mean angle of attack of $\alpha_o = 0$ deg, and an angle of attack deviation of ± 1.01 deg. We show in Fig. 15 that the airfoil designed using the multipoint approach, using five time steps per period, designated as mp 5 is almost identical to the one designed using a full unsteady optimization approach at a reduced frequency of $\omega_r = 0.01$. Figure 16 demonstrates a close-up view of the final upper surface between the 10 and 75% chord location for various design approaches. The final airfoil based on the multipoint approach using various number of time steps per period virtually produces identical profiles. As expected and seen in the previous figure, the unsteady design at a reduced frequency of 0.01 is very similar to that of the multipoint approaches. As the reduced frequency increases, the final airfoil profile departs from that produced by the simple multipoint approach. However, the differences are very small, except in areas on the upper surface, for which a greater reduction in the curvature is seen for higher reduced frequencies.

Figure 17 further supports this fact, with almost identical convergence histories of the objective function (time-averaged drag) between the various multipoint approaches and the unsteady design at $\omega_r = 0.01$. Table 4 contains a comparison of the initial and final time-averaged drag counts for the various design approaches performed at various reduced frequencies. The table further illustrates that for the four cases (mp 5, mp 11, mp 23, and $\omega_r = 0.01$), the initial time-averaged drag is approximately 147 drag counts and the final drag is 111 counts. As the reduced frequency increases, the initial drag reduces by a small amount due to nonlinear effects primarily due to the movement of the shock; however, the final drag count reduces substantially. Therefore, the three unsteady cases showcased in Table 4 and Figs. 15 and 17 represent the lower, middle, and upper limits of the reduced-frequency range. Figure 18 demonstrates the change in ΔI, where I is the objective function and ΔI converges linearly until the final airfoil profile is realized and the convergence accelerates. All design cases are automatically halted once ΔI reaches 1E-6. As illustrated in both Figs. 16 and 17, the convergence of the unsteady case at $\omega_r = 0.01$ is very similar to the multipoint cases. As the reduced frequency increases, the number of design cycles required to obtain the final design increases. We conjecture that this is due to the level of unsteadiness of the problem.

In Figs. 19 and 20, we demonstrate the comparison of the gradients between the adjoint-based multipoint and unsteady approaches. The gradients are plotted in a clockwise direction from the lower trailing edge to the upper trailing edge. Figure 19 illustrates that the gradients between the multipoint approach using 23 time steps per period are very similar to the unsteady design approach for various reduced frequencies for a majority of the grid points, except for grid points between 80 and 100, as shown in Fig. 20. This range of grid points coincides with the shock footprint and produces the dominant gradients in this design problem. The figure illustrates once again that the gradients produced by the unsteady test case at a reduced frequency of $\omega_r = 0.01$ are similar to that produced by the multipoint approach. At higher reduced frequencies, the gradients differ greatly in this range of grid points and this is largely due to the increase in the nonlinear behavior of the unsteady transonic flow.

In summary, Figs. 15–20 demonstrate that at very low reduced frequencies, the design convergence histories, final airfoil profiles,

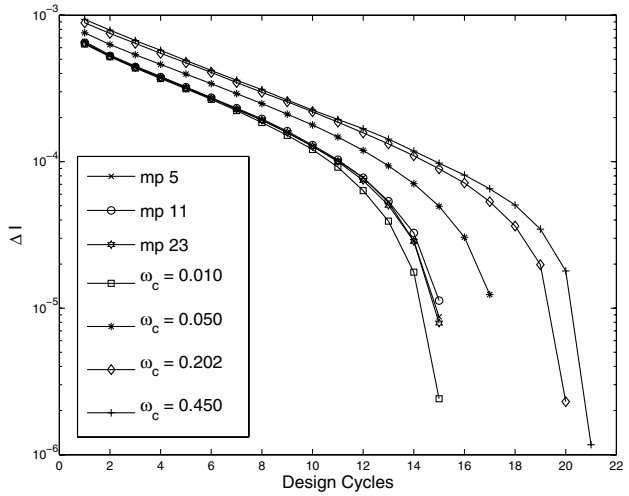

Fig. 18 Convergence of δI for various design approaches for the RAE 2822 airfoil at $M_\infty = 0.78$, $\alpha_o = 0$ deg, and fixed $C_l = 0.51$.

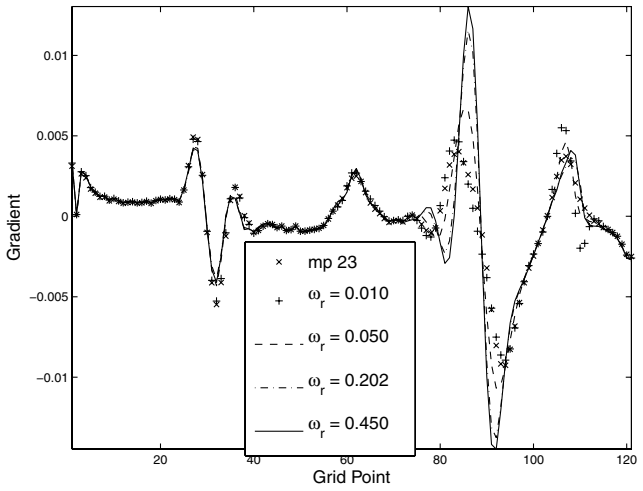

Fig. 19 Comparison between unsteady discrete adjoint gradients for various reduced frequencies and the multipoint approach for the RAE 2822 airfoil at $M_\infty = 0.78$, $\alpha_o = 0$ deg, and fixed $C_l = 0.51$.

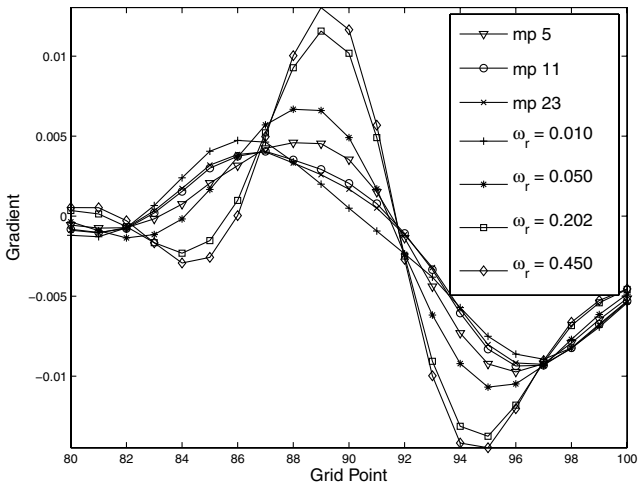

Fig. 20 Close-up view of the comparison between unsteady discrete adjoint gradients for various reduced frequencies and the multipoint approach for the RAE 2822 airfoil at $M_\infty = 0.78$, $\alpha_o = 0$ deg, and fixed $C_l = 0.51$.

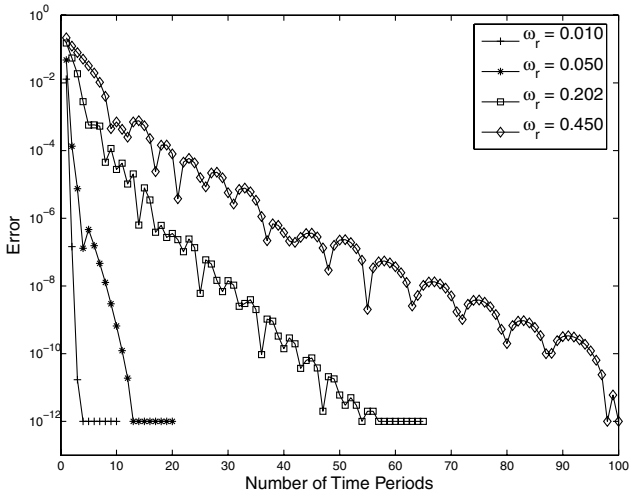

Fig. 21 Convergence of time-averaged lift coefficient for various reduced frequencies.

and gradients are very similar to that produced by a multipoint design approach. At moderate reduced frequencies between 0.05 and 0.45, however, these trends begin to deviate. The greater the nonlinear behavior of the unsteady transonic flow, the larger the difference from the multipoint approach. Figure 21 further supports this observation by illustrating the additional number of time periods required for the higher reduced frequency cases to obtain a converged time-averaged drag coefficient to machine accuracy. The additional periods are required to diminish the transient solutions due to the increase in the nonlinear behavior, to arrive at a periodic steady-state solution. The figure demonstrates that only four periods are required to obtain a converged drag coefficient at a reduced frequency of 0.01; however, 60 periods were required for the 0.20 case and 100 for the 0.45 case.

Ultimately, to compare the behavior of the final airfoil designed by the two approaches, the airfoil designed using the multipoint approach was computed using the time-accurate flow solver for the three moderate reduced frequencies. Table 5 lists the final time-averaged drag coefficients computed at a Mach number of 0.78 and at a fixed lift coefficient of 0.51. At $\omega_r = 0.05$, the difference between the unsteady and multipoint approaches is 0.2%. At a reduced frequency of 0.20 and 0.45, the difference grows to 6.4 and 8.3%, resulting in lower drag coefficients for the airfoils designed using the unsteady approach. Figure 22 illustrates a comparison of the pressure distribution at a reduced frequency of 0.45 between the airfoils designed using the multipoint and unsteady approaches. It is clearly seen that the 8.3% improvement in the drag coefficient for the unsteady technique is due to the weaker shock on the upper surface of the airfoil.

The multipoint approach certainly provides an inexpensive alternative to the unsteady design technique and has produced an optimized airfoil with a lower time-averaged drag coefficient over a range of reduced frequencies. However, if an airfoil, turbine, or rotor blade is designed for a specific range of reduced frequencies, the adjoint-based unsteady optimization technique may provide an added benefit.

VII. Conclusions

This paper presents a complete formulation of the continuous and discrete unsteady inviscid adjoint approaches to automatic

Table 5 Comparison of C_d between the multipoint and unsteady design approaches

Case	Unsteady	Multipoint	Improvement
$\omega_r = 0.05$	0.00925	0.00927	0.2%
$\omega_r = 0.20$	0.00750	0.00801	6.4%
$\omega_r = 0.45$	0.00719	0.00784	8.3%

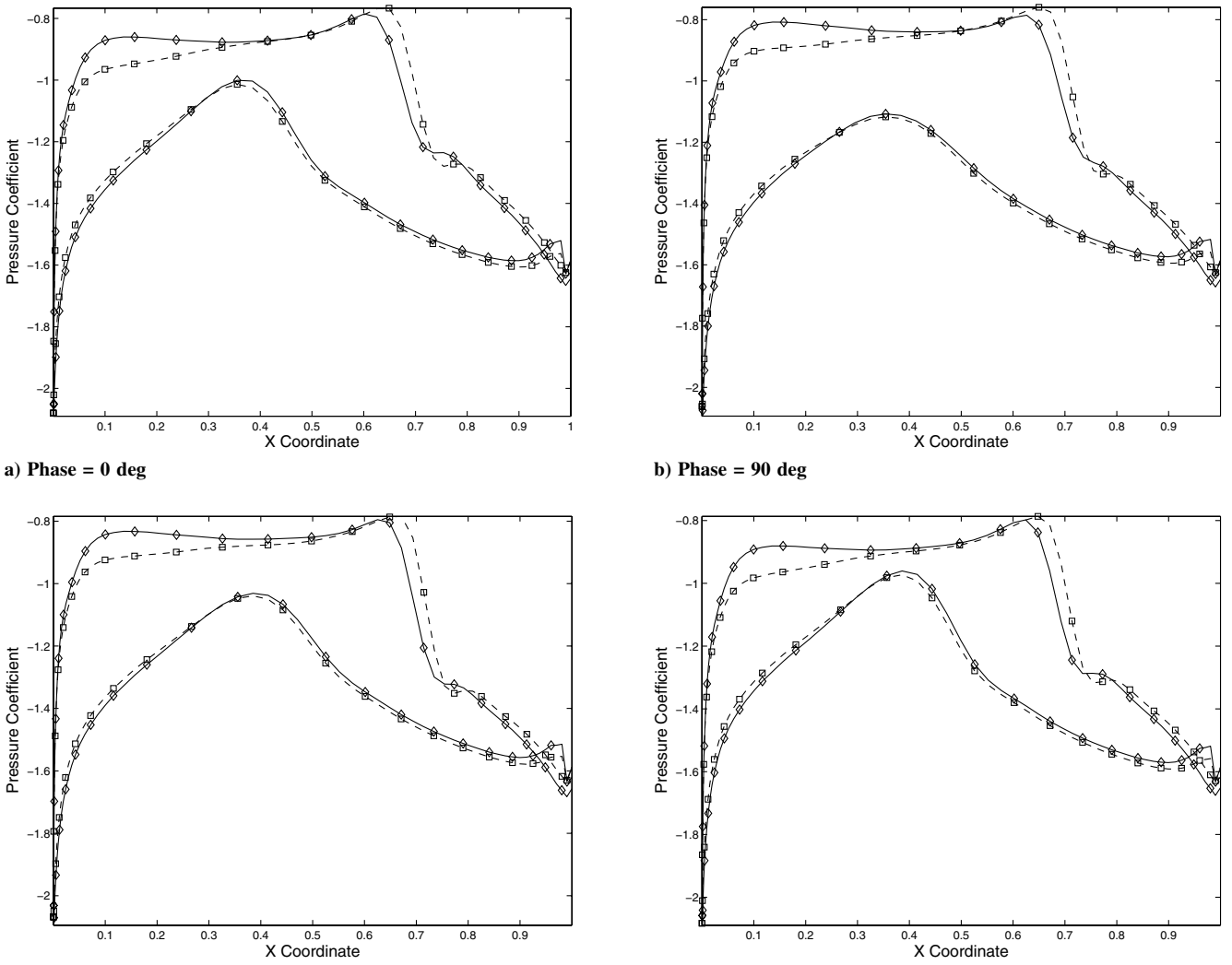

a) Phase = 0 deg

b) Phase = 90 deg

c) Phase = 180 deg

d) Phase = 270 deg

Fig. 22 Comparison of pressure distributions between airfoils designed via multipoint and unsteady approaches at various phases for the RAE 2822 airfoil at $M_\infty = 0.78$, $\omega_r = 0.45$, and $\alpha_o = 0\,\mathrm{deg}$ ($\diamond$ is unsteady and $\square$ is multipoint).

aerodynamic design. A 46% reduction in the time-averaged drag coefficient was achieved for the RAE 2822 airfoil at a reduced frequency of 0.45 while maintaining the time-averaged lift coefficient. A comparison between final airfoil profiles, convergence histories of the objective function, and gradients demonstrate that at low reduced frequencies, there is no added benefit of performing aerodynamic shape optimization for unsteady flows via an adjoint-based unsteady optimization technique; however, at moderate reduced frequencies, an unsteady optimization technique produced final airfoil profiles with time-averaged drag coefficients between 6.4 to 8.3% improvement over the multipoint approach. The framework was established to extend this method to viscous dominated flows in which secondary flow effects are present.

Acknowledgments

This research benefited greatly from the generous support of the U.S. Air Force Office of Scientific Research (AFOSR) under grant number AF F49620-98-1-022 and the Department of Energy under contract number LLNL B341491 as part of the Accelerated Strategic Computing Initiative (ASCI) program.

References

[1] Jameson, A., "Computational Aerodynamics for Aircraft Design," *Science*, Vol. 245, No. 4916, July 1989, pp. 361–371.

[2] Reuther, J., Cliff, S., Hicks, R., and van Dam, C. P., "Practical Design Optimization of Wing/Body Configurations Using the Euler Equations," AIAA Paper 92-2633, 1992.

[3] Gallman, J., Reuther, J., Pfeiffer, N., Forrest, W., and Bernstorf, D., "Business Jet Wing Design Using Aerodynamic Shape Optimization," 34th Aerospace Sciences Meeting and Exhibit, Reno, NV, AIAA Paper 96-0554, 1996.

[4] Reuther, J., Alonso, J. J., Martins, J. R. R. A., and Smith, S. C., "A Coupled Aero-Structural Optimization Method for Complete Aircraft Configurations," 37th Aerospace Sciences Meeting and Exhibit, Reno, NV, AIAA Paper 99-0187, 1999.

[5] Kasidit, L., and Jameson, A., "Case Studies in Aero-Structural Wing Planform and Section Optimization," 22nd AIAA Applied Aerodynamics Conference, Providence, RI, AIAA Paper 2004-5372, 2004.

[6] Nadarajah, S., Jameson, A., and Alonso, J. J., "An Adjoint Method for the Calculation of Remote Sensitivities in Supersonic Flow," 40th Aerospace Sciences Meeting and Exhibit, Reno, NV, AIAA Paper 2002-0261, 2002.

[7] Mavriplis, D., "Multigrid Solution of the Discrete Adjoint for Optimization Problems on Unstructured Meshes," *AIAA Journal*, Vol. 44, Jan. 2006, pp. 42–50.

[8] Soto, O., Lohner, R., and Yang, C., "An Adjoint-Based Design Methodology for CFD Problems," *International Journal of Numerical Methods for Heat and Fluid Flow*, Vol. 14, No. 6, 2004, pp. 734–759.

[9] Giles, M. B., Duta, M., Muller, J., and Pierce, N., "Algorithm Developments for Discrete Adjoint Methods," *AIAA Journal*, Vol. 15, No. 5, 2003, pp. 1131–1145.

[10] Nemec, M., Zingg, D., and Pulliam, T. H., "Multipoint and Multi-Objective Aerodynamic Shape Optimization," *AIAA Journal*, Vol. 42, No. 6, 2004, pp. 1057–1065.

[11] Mohammadi, B., and Pironneau, O., "Shape Optimization in Fluid Mechanics," *Annual Review of Fluid Mechanics*, Vol. 36, 2005, pp. 255–279.
[12] Kim, H., and Nakahashi, K., "Unstructured Adjoint Method for Navier-Stokes Equations," *JSME International Journal, Series B (Fluids and Thermal Engineering)*, Vol. 48, No. 2, May 2005, pp. 202–207.
[13] Nielsen, E., Lu, J., Park, M. A., and Darmofal, D., "An Implicit, Exact Dual Adjoint Solution Method for Turbulent Flows on Unstructured Grids," *Computers and Fluids*, Vol. 33, No. 9, 2004, pp. 1131–1155.
[14] Elliot, J., and Peraire, J., "Aerodynamic Design Using Unstructured Meshes," AIAA Paper 96-1941, 1996.
[15] Anderson, W. K., and Venkatakrishnan, V., "Aerodynamic Design Optimization on Unstructured Grids with a Continuous Adjoint Formulation," *Computers and Fluids*, Vol. 28, Nos. 4–5, 1999, pp. 443–480.
[16] Ghayour, K., and Baysal, O., "Unsteady Aerodynamics and Shape Optimization Using Modified Transonic Small Disturbance Equation," 37th Aerospace Sciences Meeting and Exhibit, Reno, NV, AIAA Paper 99-0654, 1999.
[17] Yee, K., Kim, Y., and Lee, D., "Aerodynamic Shape Optimization of Rotor Airfoils Undergoing Unsteady Motion," 37th Aerospace Sciences Meeting and Exhibit, Reno, NV, AIAA Paper 99-3107, 1999.
[18] Florea, R., and Hall, K. C., "Sensitivity Analysis of Unsteady Inviscid Flow Through Turbomachinery Cascades," 38th Aerospace Sciences Meeting and Exhibit, Reno, NV, AIAA Paper 2000-0130, 2000.
[19] Jameson, A., "Time Dependent Calculations Using Multigrid, with Applications to Unsteady Flows Past Airfoils and Wings," AIAA 10th Computational Fluid Dynamics Conference, Honolulu, HA, AIAA Paper 91-1596, 1991.
[20] Jameson, A., Schmidt, W., and Turkel, E., "Numerical Solutions of the Euler Equations by Finite Volume Methods with Runge-Kutta Time Stepping Schemes," AIAA Paper 81-1259, 1981.
[21] Nadarajah, S., "The Discrete Adjoint Approach to Aerodynamic Shape Optimization," Ph.D. Dissertation, Department of Aeronautics and Astronautics, Stanford Univ., Stanford, CA, Jan. 2003.
[22] Nadarajah, S., and Jameson, A., "Optimal Control of Unsteady Flows Using a Time Accurate Method," 9th AIAA/ISSMO Symposium on Multidisciplinary Analysis and Optimization Conference, Atlanta, GA, AIAA Paper 2002-5436, 2002.
[23] Jameson, A., and Vassberg, J. C., "Studies of Alternative Numerical Optimization Methods Applied to the Brachistochrone Problem," *Computational Fluid Dynamics Journal*, Vol. 9, No. 3, 2000, pp. 281–296.
[24] Davis, S. S., "NACA 64A010 (NASA Ames model) Oscillatory Pitching," *Compendium of Unsteady Aerodynamic Measurements*, AGARD, Rept. R-702, Neuilly sur-Seine, France, Aug. 1982.
[25] McCroskey, W. J., "Unsteady Airfoils," *Annual Review of Fluid Mechanics*, Vol. 14, 1982, pp. 285–311.

N. Alexandrov
Associate Editor